10th International Kimberlite Conference, Bangalore - 2012

10IKC-128

SEGREGATION RATE AND TRANSPORT MECHANISM OF VOLATILE-BEARING MELT IN THE DEEP MANTLE

Shatskiy*A.[1,2], Litasov K.D.[1,2], Ohtani E.[1]

[1] *Dept. of Earth and Planetary Materials Science, Graduate School of Science, Tohoku University, Sendai, Japan*

[2] *V.S. Sobolev Institute of Geology and Mineralogy SB RAS, Novosibirsk, Russia*

1. INTRODUCTION

There are many direct and indirect evidences of carbonatite and hydrous fluid/melt segregation in the deep mantle during the Earth's history. A particular example is the source regions of kimberlite and lamproite, which can originate from more than 250 km depth. On the basis of the experimental studies they would correspond to contrast volatile regimes: kimberlite clearly requires abundant CO_2 in the source , whereas lamproite requires an H_2O-rich source .

Another example is the forming medium of lithospheric diamonds. The composition of micro-inclusions in "cloudy" and "fibrous" diamonds from different localities indicates that their forming media were represented by ultrapotassic super-critical fluid with different H_2O/CO_2 ratios [1]. Indeed, high-pressure experiments at 6-7.5 GPa confirm that water-bearing alkali carbonates and CO_2-H_2O fluid are the most probable media, which are capable to initiate diamond crystallization at the conditions of lithospheric mantle [2].

Since the average concentrations of carbon and hydrogen in primitive mantle would not exceed 100 and 120 wt ppm, respectively [3], the volatile segregation over a broad mantle region should be involved to explain the local abundance of CO_2 and/or H_2O. Significant enrichment of such fluids in incompatible trace elements also implies their long infiltration history through the large volumes of mantle rocks. However, mechanisms and forces driving fluid transport and segregation in the deep mantle are poorly understood.

The majority of models considers partially molten matrix, in which buoyancy driven upward percolation of melt occurs through the interconnected interstices [4], wherein the melt flux is resisted by deformation of silicate rock, which occurs by solid-state diffusion [5]. In this model the melt is poor solvent of solid and/or does not wet grain boundaries. That is understood that the melt is poor solvent of solid and/or does not wet grain boundaries. Although this is good approximation for the melt segregation in the shallow mantle (e.g. basalts in the asthenosphere), this approach cannot be directly applied for hydrous fluid and carbonatite melt segregation, because at mantle PT-conditions they are excellent silicate solvents and exhibit enhanced wetting properties . In addition, the porous flow model faces obvious difficulties to explain fluid segregation in the case of the lack of interconnectivity, i.e. in the case of trace amounts of fluid dispersed in the crystalline framework [6].

In contrast, dispersed fluid droplets can infiltrate through the crystalline framework by a dissolution-precipitation mechanism, wherein migration proceeds due to silicate dissolution ahead and crystallization astern [7]. Among the variety of driving forces promoting fluid migration by the dissolution-precipitation only a capillary force has been studied extensively concerning to the mantle [8]. In fact, this force would counteract the melt segregation. The force driving directional fluid flow such as nonhydrostatic stress [9,10] are required.

In this paper we measured $MgSiO_3$ and Mg_2SiO_4 flux through carbonatite melt and hydrous fluid layers in the thermal gradient field under transition zone and lower mantle conditions. Using obtained data we calculated silicate diffusivity in the melt/fluid and estimated possible migration rates of dispersed fluid/melt droplets in the deep mantle by means of dissolution-precipitation driven by non-hydrostatic stress.

2. EXPERIMENTAL APPROACH

In the melt infiltration process, the flux follows the general relation: Flux = (Permeability) × (Driving force). To accommodate the flux of the equilibrium melt into the nonporous solid aggregate, an equal counterflux of solid must exist. The permeability is determined by either diffusive or convective mass transfer of solute through fluid or by crystal growth kinetics. To study melt migration we used thermal gradient as a driving force (Fig. 1).

The diffusive flux can be expressed using Fick's first law as

$$f_D = D\frac{C_S' - C_i'}{l}, \qquad (1)$$

where D is the diffusion coefficient and l is the width of the solution layer, C_i' and C_S' are solute concentration [in mol/m^3] at the high-temperature side (dissolution region) and low-temperature side (growth region). The overall solute counterflux is not determined by bulk transport only, but proceeds by combined dissolution of source, diffusive mass transport, and subsequent crystal growth. Since the dissolution is generally controlled by volume diffusion , it can be omitted from the consideration. Hereinafter the "crystal growth" implies complex process including: (i) diffusion of the solvated molecules through a concentration boundary layer around growing crystal, (ii) diffusion of absorbed solvated molecules along crystal surface toward active growth centers, and (iii) incorporation of the molecules into the crystal lattice. The crystal growth component can be expressed by an empirical equation of power-law form as

$$f_G = k(C_i - C_E)^q, \qquad (2)$$

where k is the overall rate constant, C_i and C_E are the actual and equilibrium solute concentrations [in wt fraction] in the cool part of the sample chamber, and q is the order of the kinetic reaction of crystal growth, which usually varies between 1 and 2.

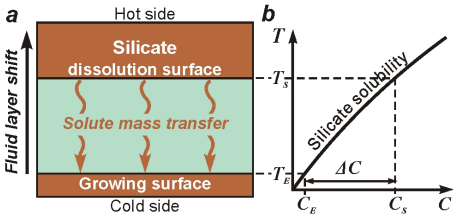

Fig. 1. Melt layer movement through the solid silicate by means dissolution-precipitation driven by silicate solubility difference in thermal gradient field, $\Delta C = C_S(T_S) - C_E(T_E)$.

Experimentally the overall solute flux can be estimated at steady state conditions from the increase of the amount of solid, dm, transported over period of time, dt, through the cross-section area of the capsule, A:

$$f = \frac{dm}{A \cdot dt} \qquad (3)$$

At steady state conditions, the flux of solute molecules through the bulk solution is equal to the crystal growth component, $f_D = f_G = f$. To extrapolate the rate obtained in the experiments at high supersaturation to that in the mantle, we assume that the migration rate is limited by the diffusion step, $q = 1$, rather than by the surface reaction step, $q > 1$ in Eq. 2. The validity of this assumption is discussed in the Section 5.2.

3. EXPERIMENTAL PROCEDURE

Experiments were conducted using a scaled-up Kawai-cell and USSA-5000 ton press [11]. Experimental procedures were the same as described in our previous papers [12,13]. The axial thermal gradient across the sample was estimated to be 20±5 ºC/mm at 1500 ºC. The composition of the starting materials is shown in Table 1.

The weight of starting materials and recovered silicate crystals and source was measured using balance with the accuracy of ±0.01 mg. The weight of recovered silicate crystals and source was also confirmed by estimation of their volumes inferred from linear dimensions measured using SEM images. Silicate solubility was calculated from the initial weight of solvent and silicate source and total weight of recovered silicate crystals. The obtained phases were identified using a microfocused X-ray diffractometer and electron microprobe analyzer.

4. EXPERIMENTAL RESULTS

Results are shown in Table 1 and illustrated in Fig. 2.

Table 1. Experimental results on silicate recrystallization through solution layer in thermal gradient filed (TG = 20 °C/mm)

Run	Experimental conditions: Solvent	Source	P, GPa	T, °C	τ, min	Recovered: C, wt.%	d, mm	M, mg: HT	M, mg: LT	Calculated: l, mm	C_e, wt.%	f, g/s/cm^2
1	KMC	Forsterite	16.5	1700	115	62	1.9	11.3	0.1	0.94	22.5	4.442×10^{-7}
2					155	55	1.9	10.8	0.4	1.21	23.3	4.550×10^{-6}
3					240	59	1.9	10.8	1.8	1.32	24.5	9.405×10^{-6}
4					450	64	1.9	4.9	6.7	0.92	28.3	1.390×10^{-5}
5					480	64	1.9	3.9	7.4	0.95	30.0	1.360×10^{-5}
6	KMCH	Enstatite	24	1500	50	70.1	1.9	12.2	0.2	0.93	30.5	2.536×10^{-6}
7					120	73.6	1.9	12.8	2.5	0.79	34.2	1.889×10^{-5}
8					180	68.9	2.0	8.4	5.0	1.06	31.1	2.237×10^{-5}
9					260	68.9	1.9	5.2	8.2	0.95	31.0	2.319×10^{-5}
10	H_2O				20	87.4	1.8	2.1	9.6	1.30	73.2	$\geq3.080\times10^{-4}$
11					60	90.4	1.8	0	11.0	1.27	78.3	$>1.175\times10^{-4}$
12				1350	16	82.2	1.8	5.3	5.3	1.00	47.2	$\geq2.139\times10^{-4}$
13					45	83.9	1.75	0	11.9	0.80	49.0	$>1.556\times10^{-4}$

τ – run duration; C –silicate concentration in system; d – sample diameter; M – weight of silicate remaining at HT side and that recrystallized in LT side; l – thickness of solvent layer; C_e – silicate solubility in solvent; f – solute flux; KMC – $K_2Mg(CO_3)_2$; KMCH – $K_2Mg(CO_3)_2\times2H_2O$.

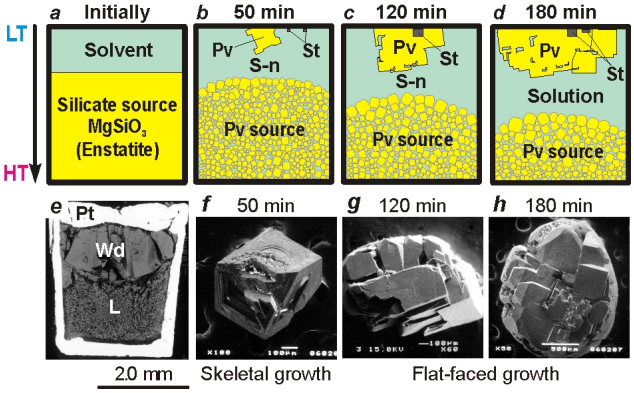

Fig. 2. Illustration of $MgSiO_3$ perovskite recrystallization though the solution layer at 24 GPa, 1500°C and TG = 20°C/mm in $K_2Mg(CO_3)_2\times2H_2O$ solvent. (***a***) Initial sample design. (***b-d***) Crystallization schemes. (e) Pots experimental sample cross-section. (***f-h***) Perovskite crystals.

5. DISCUSSION

5.1. Steady and unsteady state mass transfer

Steady state can be established when the area of growing crystals and dissolving source are larger or equal to the area of the capsule cross-section. In terms of this

criterion following time intervals can be defined for the steady state mass transfer: 240-480 min for Mg_2SiO_4 in KMC at 16.5 GPa and 1700°C, 180-260 min for $MgSiO_3$ in KMCH at 24 GPa and 1500°C, and ≤ 20 min for $MgSiO_3$ in H_2O at 24 GPa and 1500°C. The maximum possible unsteady state period for the last system can be estimated from the time needed to expand the growing crystal surface to the cross-section area of the capsule. Assuming negligibly short induction period preceding nucleation and time independent perovskite growth rate, the unsteady state period does not exceed 5 min. However, the actual value should be somewhat less since an average growth rate during unsteady state exceeds a growth rate estimated from single run, where mass transfer proceeded at unsteady and than at steady state (Fig. 3).

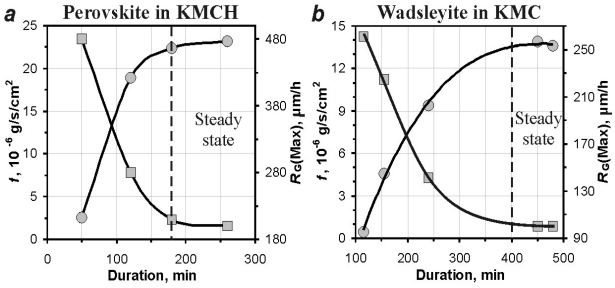

Fig. 3. Changes of silicate flux, f (circles), and maximum crystal growth rate, $R_G(Max)$ (squares), with time. Silicate recrystallization was carried out through the solution. (a) $MgSiO_3$ perovskite growth in $K_2Mg(CO_3)_2$×$2H_2O$ solvent at 24 GPa and 1500°C. (b) Mg_2SiO_4 wadsleyite growth in $K_2Mg(CO_3)_2$ solvent at 16.5 GPa and 1700°C.

The surface area coverage is a necessary but insufficient criterion. Therefore, time dependence of silicate flux, f, and growth rate, $R_G(Max)$, was studied in the experiments with various duration. As illustrated in Fig. 3, f increases and $R_G(Max)$ decreases rapidly with time achieving nearly constant values at certain run duration, namely ~200 min in KMCH and ~400 min in KMC. The cause of the observed dynamics can be illustrated as follows. In the beginning of a run at time after achieving critical concentration in the cool region, i.e. $C_i > C_{3D}$, the nucleation occurs (Fig. 4a). Even negligible amount of material consumed on the formation of

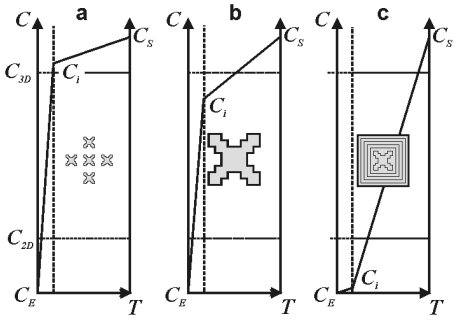

Fig. 4. Expected evolution of solute concentration profiles along the solution layer sandwiched by the hot dissolving and cool growing silicate layers at unsteady (a, b), and steady (c) state conditions. (a) Spontaneous nucleation. (b) Skeletal growth. (c) Flat faceted growth. C_S – the solute concentration near silicate source or equilibrium silicate solubility in the hot region; C_i – the actual solute concentration in the cool region; C_E – the equilibrium silicate solubility in the cool region; C_{3D} – the supersaturation required for spontaneous nucleation; C_{2D} – the supersaturation separating the region of skeletal growth and flat-faceted growth.

1 to 5 crystallites is sufficient to decrease C_i below C_{3D}, which terminates further nucleation (Fig. 4b). While the crystals are small, the diffusion distance of solvated molecules to crystal facets from the supersaturated melt is small. Accordingly, the growth rate is maximal. The small diffusion pass of solvated molecules causes inhomogeneous concentration of solute around the crystal (higher at corners and edges and lower near facets). As a result skeletal growth occurs. As the silicate components diffuse from the bulk melt (not from the source), their diffusion length increases until it become equal to the distance from the source to the crystals. After this point the steady state mass transfer is established.

5.2. Mass transfer limiting step

Either crystal growth or volume diffusion becomes the slowest step, which predominantly determines the overall solute flux. In our experiments the bulk supersaturation exceeds that required for spontaneous nucleation, i.e. $C_S > C_{3D}$ (Fig. 4). Otherwise, crystallization would not occur because we did not use seed crystals. At steady state, we observed the flat-facet growth (Fig. 2g,h). This morphology corresponds to the low supersaturation near crystal/solution interface, i.e. $C_E < C_i << C_{2D}$ (Fig. 4c). Hence, the solute concentration in the cool region is significantly lower than that, which can be potentially established, $C_i > C_S$ (Fig. 4c). It means that crystals grow fast enough to consume all solute delivered from the source. Although negligibly low driving force of growth, $C_i - C_S << C_{2D} - C_E$, it easily compensates diffusion mass transfer, which is driven by much larger concentration difference, $C_S - C_i \approx C_{3D} - C_E$ (Fig. 4c). This suggests low D/k ratio (Eq. 1, 2). Consequently, the volume diffusion mass transfer predominantly resists the overall solute flux at steady state in our experiments.

5.3. Silicate diffusivity

In the case of the thermal gradient driving force, the diffusive flux can be expressed through the slope of silicate solubility curve and thermal gradient,

$$f_D = D \times \left(\frac{dC'}{dT}\right) \times \left(\frac{dT}{dl}\right). \quad (4)$$

Thus, combination of Eq. 4 and silicate flux estimated experimentally at steady state using Eq. 3, enables extraction of diffusivity. Silicate solubility was estimated from the mass of initial silicate source and solvent and the mass of recovered source and grown crystals, $C_e = M_{silicate}^{dissolved} / \left(M_{silicate}^{dissolved} + M_{solvent}^{initial}\right)$, where $M_{silicate}^{dissolved} = M_{source}^{initial} - \left(M_{source}^{recov.} + M_{crystals}^{grown}\right)$. We neglect the slight deviation of solute composition in hydrous melt and KMCH from $MgSiO_3$ stoichiometry (Mg/Si ~1.15 [12]) assuming congruent dissolution. The slopes of silicate solubility curves were estimated from our unpublished experimental

data and estimated melting points of water (600°C at 24 GPa [14]), $MgSiO_3$ (2280°C at 24 GPa [15]), and Mg_2SiO_4 (2200°C at 16.5 GPa [15]). To calculate molar concentration, density of solution, $\rho_{solution}$, at given pressure and temperature,

$$C' = \frac{C_{solute}/M_{solute}}{100/\rho_{solution}}, \quad (5)$$

has to be known. Density of hydrous melt was estimated from known silicate solubility and HPHT density data of hydrous and dry $MgSiO_3$ melt [16] assuming linear temperature- and water concentration-density dependences. Densities of hydrous and dry carbonatite melts were calculated from the density of $MgSiO_3$±H_2O melt [16] and the partial molar volume of CO_2 [17]. The latter was corrected to the partial molar volume of CO_2 at 1500 and 1700°C using the thermal expansion data at ambient pressure [18]. The density estimates are summarized in Table 2. The accuracy of estimating silicate weight (±0.01 mg), recovered capsule diameter (±15 %), solubility slope (±40 %), and thermal gradient (±50 %) would lead to a ±60 % error in *D*.

Table 2. Estimates of silicate solubility and diffusive transport in carbonate melt and hydrous fluid at mantle *PT* conditions

Solvent	KMC		KMCH		H_2O		
Silicate	Mg_2SiO_4		$MgSiO_3$		$MgSiO_3$		
P, GPa	16.5		24		24		
T, °C	1600’	1700	1500	1700”	1350	1500	1700”
C_e, wt%	16.8	25.7	31.7	47.4	48.1	75.7	88.8
$\rho_{solution}$, g/cm^3	3.00	3.02	3.23	3.29	1.99	2.94	3.39
C_e’, ×10^{3}mol/m^3	3.59	5.52	10.2	15.5		22.2	30.0
dC/dT, wt%/°C	0.09	0.10	0.09	0.11	0.28	0.11	0.05
f, ×10^{-3} mol/m^2/s	-	1.0	2.3	-	21	31	-
D, ×10^{-9} m^2/s	2.0	2.4	3.9	5.6	≥19	≥50	≥71

* - Diffusivity was estimated assuming the same activation energy as reported for CO_3^{2-} in carbonate melt, 48 kJ/mol (see capture Fig. 11 for the references). ** - Diffusivity was estimated assuming the same activation energy as reported by [19] for SiO_2 diffusion in H_2O at 1 GPa, 52 kJ/mol. KMC – $K_2Mg(CO_3)_2$; KMCH – $K_2Mg(CO_3)_2$×$2H_2O$.

The obtained diffusivities are listed in Table 2 and presented in Fig. 5, which also includes the lower pressure data for SiO_2 diffusivity in silicate melt and hydrous fluid and CO_3^{2-} diffusivities in carbonate melt. Note that in contrast to the solid and polymerized liquid, the diffusion coefficients of different elements in the depolymerized melt/fluid are very similar, i.e. coincide within one order of magnitude . In accordance with our results the silicate diffusivity varies in the following sequence: H_2O > $K_2Mg(CO_3)_2$×$2H_2O$ > $K_2Mg(CO_3)_2$ (Fig. 5). Extrapolation of SiO_2 diffusivity in a hydrous supercritical fluid measured at pressure of 1 GPa and temperatures up to 1500°C [19] gives one order of magnitude higher diffusivity than that of $MgSiO_3$ in hydrous melt at 1500°C and 24 GPa (Fig. 5). It can be attributed to the higher silica concentration in hydrous melt/fluid in our study (~26 mol.%) than that in [19] (≤ 4 mol.%). Silica polymerization in the fluid depends strongly on the bulk SiO_2 concentration. At the concentration level below 20 mol.% SiO_2, H_4SiO_4 monomers and $H_6Si_2O_7$ dimers are the major silica species, whereas at the concentrations above 20 mol.% SiO_2 they are replaced by higher oligomers [20].

The diffusivity of CO_3^{2-} in carbonate melt at 1 atm also exceeds that of Mg_2SiO_4 in KMC melt at 16.5 GPa by an order of magnitude (Fig. 5). This difference can be explained as follows. The carbonate melt has flexible atomic structure , which diminishes diffusivity difference between contrast diffusant . However, addition of more than 33 mol.% silica into carbonate melt leads to the polymerization of silicon tetrahedra [21]. Therefore, the diffusivity difference between our and previous data would be attributed to the identity of the diffusant and more rigid atomic structure of carbonatite melt containing 38 mol.% SiO_2. The pressure effect on the carbonatite melt structure, which can be expected by the analogy with phase transitions in solid carbonates can be considered as an another reason for observed diffusivity difference [22].

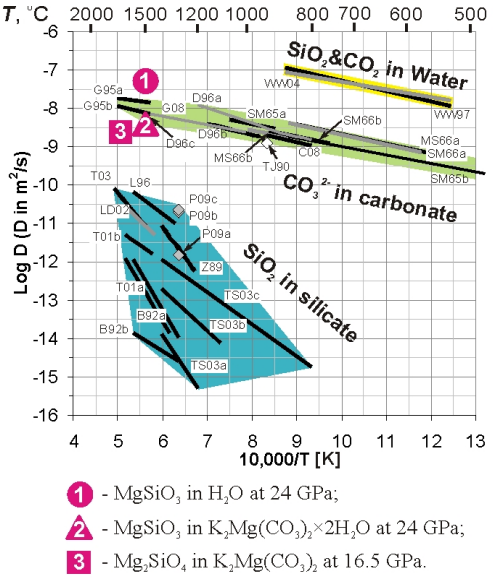

Fig. 5. Arrhenius diagram showing silicate diffusivity in hydrous (1), hydrous carbonatite (2), and carbonatite melts (3) obtained in this study at transition zone and lower mantle pressures. Literature data on the diffusion characteristics of hydrous supercritical fluid and hydrous silicate, “dry” silicate, and carbonatite melts obtained at shallow mantle and ambient pressures are shown for the comparison.

5.4. Melt segregation in the deep mantle

Although silicate diffusivities in hydrous and carbonatite melt are high, the silicate flux and therefore migration rate in the real Earth’s mantle conditions are essentially determined by the driving force, i.e. concentration difference (Eq. 1). The latter can be caused by nonhydrostatic stress in convective mantle, which is estimated in the range of 0.1-10 MPa. In this section we estimate the melt migration rates driven by these forces.

Dissolution/precipitation of solids is fully described by the surface chemical potential, μ. If a nonhydrostatic stress, σ, affects the solid particle in addition to the hydrostatic pressure, the chemical potential in the solid is increased by

$$\Delta\mu = V_m\sigma, \quad (6)$$

where *Vm* is the molar volume of solid [9]. Mineral solubility at stressed state is given by

$$C' = C_e'\exp(\Delta\mu/RT) = C_e'\exp(V_m\sigma/RT), \quad (7)$$

Where C_e' is the mineral solubility (solute molar concentration) at zero stress and *R* is the gas constant [9,23]. This expression has been derived previously by [24]. Thermodynamic considerations [25] show that this approximation is valid not only for the solubility of a mineral in the bulk fluid but also in thin intergranular films existing due to the disjoining pressure. Combining Eqs. 1 and 7 the stress-driven diffusive flux can be expressed as:

$$f_D = \frac{DC_e'}{l}\left(\exp\left(\frac{\sigma V_m}{RT}\right) - 1\right). \quad (8)$$

Due to this distribution of concentration in the liquid phase, the crystal is dissolved in a strained zone and the dissolved material diffuses through the liquid and crystallizes at a sink outside the strained contact. This kind of process has been demonstrated by the movement of brine in a KCl crystal in a stress gradient [10].

The thickness of melt droplet, *l*, was chosen in the range from 0.001 to 0.1 mm according to the size of syngenetic fluid/melt inclusions in mantle xenoliths. The rates of melt migration estimated form the flux driven by stress are presented in Fig. 6.

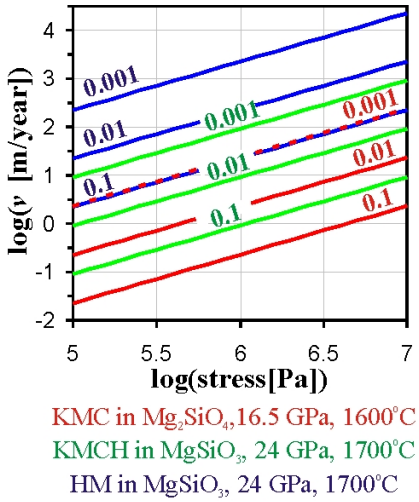

Fig. 6. Stress dependent rate of fluid moving through non-porous solid silicate mantle by means of stress-driven dissolution-precipitation mechanism. Numbers are diffusion path length (i.e. fluid inclusion size or thinness of fluid film). Fluid compositions (silicate solubility) are given in Table 2. HM denotes hydrous melt.

As can be seen both melt droplet size and stress have substantial effect on the migration rate. At typical mantle stress of 1 MPa and droplet size or fluid film thickness of 10 μm the migration rate of hydrous and KMCH melts is estimated to be 225 and 9 m/year, respectively, at 24 GPa and 1700°C. In the case of KMC melt at 16.5 GPa and 1600°C the migration rate is near 2 m/year. For comparison the rates of mantle upwelling (ascent plume) would not exceed several centimeters per year , which is 2-4 orders of magnitude slower than the proposed melt migration rates.

To conclude, the melt formation and rock deformation coexist in time and space on a large scale. It is proposed that melting in Earth's mantle occurs primarily in plumes, which are regions of intense deformation [4]. Our data suggest that the dispersed hydrous or carbonatite melt/fluid could rapidly segregate within oxidized domains of the upwelling mantle by means of stress-driven dissolution-precipitation mechanism. This mechanism may explain early stage of segregation of mantle magmas with source regions deeper than 150-250 km. Furthermore, if the melt/fluid and the silicate matrix were not at chemical equilibrium in respect to trace elements, as would be the case in the mantle, dissolution and precipitation reactions would result in a very efficient exchange of these components between the melt and the matrix.

REFERENSES

1 Schrauder, M. *et al. Geochimica Et Cosmochimica Acta* **58**, 761-771 (1994).
2 Pal'yanov, Y. N. *et al. Nature* **400**, 417-418 (1999).
3 McDonough, W. F. in *Treatise on Geochemistry* Vol. 2 (eds H. D. Holland *et al.*) 547-568 (Oxford: Elsevier – Pergamon., 2003).
4 Kohlstedt, D. L. *et al. Annual Review of Earth and Planetary Sciences* **37**, 561-593, doi:10.1146/annurev.earth.031208.100104 (2009).
5 Cooper, R. F. *et al. Tectonophysics* **107**, 207-233 (1984).
6 McKenzie, D. *Earth and Planetary Science Letters* **74**, 81-91 (1985).
7 Whitman, W. G. *American Journal of Science* **11**, 126-132 (1926).
8 Hammouda, T. *et al. Geology* **28**, 283-285 (2000).
9 Kruzhanov, V. *et al. Pure and Applied Geophysics* **152**, 667-683 (1998).
10 Geguzin, Y. E. *et al. Kristallografiya* **24**, 866-867 (1979).
11 Shatskiy, A. *et al. Physics of the Earth and Planetary Interiors*, doi:10.1016/j.pepi.2011.1008.1001, doi:10.1016/j.pepi.2011.08.001 (2011).
12 Shatskiy, A. *et al. American Mineralogist* **92**, 1744-1749, doi:10.2138/am.2007.2415 (2007).
13 Shatskiy, A. *et al. American Mineralogist* **94**, 1130-1136, doi:10.2138/am.2009.3150 (2009).
14 Katayama, Y. *et al. Physical Review B* **81**, doi:014109 10.1103/PhysRevB.81.014109 (2010).
15 Liebske, C. *Mantle-Melting at High Pressure-Experimental Constraints on Magma Ocean Differentiation* Doktors der Naturwissenschaften thesis, Universität Bayreuth, (2005).
16 Mookherjee, M. *et al. Nature* **452**, 983-986 (2008).
17 Ghosh, S. *et al. Geophysical Research Letters* **34**, L22312, doi:10.1029/2007GL031349 (2007).
18 Liu, Q. *et al. Mineralogy and Petrology* **146**, 370-381 (2003).
19 Watson, E. B. *et al. Contributions to Mineralogy and Petrology* **130**, 66-80 (1997).
20 Newton, R. C. *et al. Earth and Planetary Science Letters* **274**, 241-249 (2008).
21 Treiman, A. H. *et al. Journal of Geology* **91**, 437-447 (1983).
22 Cancarevic, Z. P. *et al. Chemistry-a European Journal* **13**, 7330-7348, doi:10.1002/chem.200601637 (2007).
23 Chernov, A. A. *Progress in Crystal Growth and Characterization of Materials* **26**, 121-151 (1993).
24 Elliott, D. *Geological Society of America Bulletin* **84**, 2645-2664, doi:10.1130/0016-7606(1973)84<2645:dflimr>2.0.co;2 (1973).
25 Heidug, W. K. *Journal of Geophysical Research-Solid Earth* **100**, 5931-5940, doi:10.1029/94jb03100 (1995).